Free Radical Biology and Medicine 199 (2023) 166–176

Contents lists available at ScienceDirect

Free Radical Biology and Medicine

journal homepage: www.elsevier.com/locate/freeradbiomed

Ultrasound sensitive O_2 microbubbles radiosensitize murine breast cancer but lead to higher metastatic spread

Agnieszka Drzał [a], Anthony Delalande [b,d], Gabriela Dziurman [a], Chantal Pichon [b,c,d], Jan Swakoń [e], Martyna Elas [a,*]

[a] Jagiellonian University, Faculty of Biochemistry, Biophysics and Biotechnology, Department of Biophysics and Cancer Biology, Kraków, Poland
[b] University of Orleans, 45067, Orleans, France
[c] Institut Universitaire de France, 75231, Paris, France
[d] Center for Molecular Biophysics, CNRS Orleans, 45071, Orleans, France
[e] Institute of Nuclear Physics, Polish Academy of Sciences (IFJ PAN), Krakow, Poland

ARTICLE INFO

Keywords:
Oxygen microbubbles
Hypoxia
Radiotherapy
EPR imaging

ABSTRACT

The inadequate level of oxygenation in tumors has been shown to correlate not only with greater invasiveness of cancer cells, but also with a reduction in their sensitivity to anticancer therapies. Over the years, many attempts have been made to increase the oxygenation level of cancer, but most of them have been ineffective. We investigated the heterogeneous response of tumor tissue to phospholipid-coated oxygen microbubbles (OMB) in murine tumors *in vivo* using oxygen and hemoglobin saturation mapping and the influence of OMB treatment on microvasculature, perfusion, and radiotherapy effectiveness. Intravenous administration of OMB followed by ultrasound pulse leads to increased oxygenation of a tumor, found mainly in the vicinity of tumor vessels, while intratumoral delivery resulted in areas of increased pO_2 more evenly distributed within the tumor. Furthermore, hemoglobin contributes little to the increase in tumor oxygenation caused by oxygen microbubbles. Extensive vasculature disruption was observed in the groups treated with both oxygen/nitrogen microbubbles and ultrasound pulse. This therapy also led to a reduction in the coverage of the vessels by pericytes, while the density of the microvessels was unchanged. Radiotherapy with a single dose of 12Gy reduced tumor growth by 50% in all treated groups. Unfortunately, at the same time, the number of macroscopic metastases in the lungs increased significantly after intravenous administration of oxygen/nitrogen microbubbles and the application of an ultrasound pulse. In conclusion, ultrasound-sensitive oxygen microbubbles are effective in delivering oxygen to tumor tissue, thus increasing the effectiveness of radiotherapy. However, cavitation effects and destruction of the integrity of tumor vessels result in greater spread of cancer cells in the host organism.

1. Introduction

Reduced oxygen availability, known as hypoxia, is a hallmark of the tumor microenvironment [1]. This biological phenomenon was first described in lung cancer by Thomlinson and Gray in the 1950s [2]. It is well established today that hypoxia occurs in almost all solid tumors. Approximately 50–60% of tumor regions show significantly lower levels of O_2 than the tissues from which they originate [3]. Although the presence of hypoxia within the tumor is independent of its stage or histology, hypoxia regulates many pathological processes that favor the development of a more malignant phenotype and is correlated with poor clinical outcomes in patients [4]. Hypoxia has been shown to influence the invasive and migratory behavior of cancer cells by stimulating the epithelial-mesenchymal transition (EMT), enabling plastic and invasive abilities [5]. Increased expression of EMT markers such as N-cadherin, β-catenin, TWIST and Snail is correlated with low oxygenation and worse prognosis in patients [6].

The dependence of tissue and cell response to low linear energy transfer (LET) ionizing radiation on the level of oxygen has been known since the seminal work of Schwarz [7]. It is quantified as the oxygen enhancement ratio (OER). For most cells in culture, the OER between anoxia (ie complete oxygen deprivation during irradiation) and air (160

* Corresponding author. Dept. Biophysics and Cancer Biology, Faculty of Biochemistry, Biophysics and Biotechnology, 7 Gronostajowa St., 30-387, Kraków, Poland.
E-mail address: martyna.elas@uj.edu.pl (M. Elas).

https://doi.org/10.1016/j.freeradbiomed.2023.02.022
Received 16 December 2022; Received in revised form 6 February 2023; Accepted 24 February 2023
Available online 27 February 2023

mmHg or 21% oxygen) is between 2.5 and 3 [8]. The largest change in radiosensitivity, that is, the highest OER, occurs in the range of oxygen partial pressure between 0.5 and 15 mmHg (0.05–2.5%), and an increase above 15 mmHg leads to only minor changes in radiation sensitivity. It should be noted that the effect of oxygen enhancement can be observed only when molecular oxygen is present just before irradiation or within microseconds of exposure [9].

Many cancer treatment strategies depend on oxygen. That is why its low concentration in tumor tissues limits the effectiveness of chemotherapy, immunotherapy, photodynamic therapy, and radiotherapy [10]. Due to the recognition of hypoxia as an important barrier in cancer treatment, various measures have been taken to overcome or reverse tumor hypoxia. In the 1930s, the first tests of the administration of oxygen for breathing were performed [11]. Today, such approaches also include hyperbaric oxygen respiration, hemoglobin-based oxygen carriers and allosteric modifiers, perfluorocarbon-based carriers, and microbubbles of oxygen [12–16].

Microbubbles (MBs) have become an important area of biomedical research due to their wide diagnostic and interventional applications [17–20]. An important property of microbubbles is ultrasound-induced cavitation, which can take the form of inertial or non-inertial cavitation [21]. Both types of cavitation can generate micro-jets, or hydrodynamic shock waves, in the surrounding environment, which can damage cell membranes [22]. These effects can cause changes in vascular permeability and apoptosis of endothelial cells. In the context of tumor vasculature, the effect of enhanced permeation and retention, resulting from the leakage and pathological structure of these vessels, has been reported [23].

The use of ultrasound-sensitive oxygen-filled microbubbles (OMBs) has also been explored for several years. Recently, our group has shown that anionic pegylated OMBs composed of distearoylphosphatidylcholine (DSPC) and PEGylated 1,2-distearoyl-sn-glycero-3-phosphorylethanolamine (DSPE-PEG2000) are an efficient and non-toxic way to increase tumor oxygenation [24]. Using a sensitive and quantitative technique to measure oxygen (electron paramagnetic resonance, EPR) we determined that the increase in pO_2 lasts *in vivo* for approximately 15–20 min after microbubble disruption and leads to a decrease in hypoxia-inducible factor 1α (HIF-1α) and vascular endothelial growth factor A (VEGF-A) in cancer cells at both the levels of mRNA and protein. Here, we further investigated the applications of oxygen microbubbles in cancer therapy. We characterized the heterogeneous response of tumor tissue to OMB treatment with the use of both EPR oximetric and photoacoustic imaging and studied their effectiveness as a radiosensitizer *in vivo*. Additionally, we evaluated the vascular consequences of microbubble cavitation and their role in the metastasis process.

2. Materials and methods

2.1. Microbubbles formulation and disruption

A liposomal formulation of DSPC:DSPE-PEG2000 (0.9:0.1 M ratio) was prepared as previously described [24]. Briefly, 5 mg/ml lipid solution in HEPES buffer (Gibco, Thermo Scientific, USA) was freeze-dried and the headspace of the vial was replaced by C_4F_{10} gas (F2 Chemicals, UK). Before the experiments, the perfluorocarbon was replaced with oxygen, the vial content was resuspended in 500 μl of HEPES buffer and activated by mechanical agitation using a VialMix (Bristol-Myers Squibb) for 45 s. Microbubbles were destroyed using a Vevo Sonigene device (VisualSonics, Canada) sending ultrasound at 1 MHz at 2 W/cm^2 for 1 min. Attention was taken to use microbubbles no later than 30 min after activation.

2.2. Animals and tumor model

4T1 cells were grown at 37 °C in a humidified atmosphere of 5% CO_2/95% air in RPMI 1640 (Sigma Aldrich, USA) containing 10% heat-inactivated fetal bovine serum (Gibco, Thermo Scientific, USA) plus penicillin-streptomycin (Sigma Aldrich, USA) under sterile tissue culture conditions.

Balb/c female mice at the age of 3 months were originally obtained from the animal breeding facility at the Medical University of Bialystok (Bialystok, Poland). All experimental procedures were approved by the First Local Ethic Committee of Cracow (Permission No. 36/2016). The mice were housed under standard laboratory conditions LD:12/12, humidity: 60%, temperature: 23°C. The standard food diet with free access to drinking water was provided in community cages.

For each mouse, $5x10^5$ 4T1 cells, suspended in 50 μl of PBS, were injected into the mammary fat pad. In vivo evaluation of OMB effectiveness (by EPR and photoacoustic imaging) and radiotherapy was performed when the tumors were approximately 6 mm in diameter (7 days after tumor implantation). Three separate animal cohorts (EPR imaging, photoacoustic, and radiotherapy), each consisting of 48 mice, were used with different endpoints: euthanasia after either 3h or 24h, or until the development of metastasis. The same experimental groups were used in each cohort, N = 8 in each experimental group.

2.3. In vivo EPR measurements

In vivo EPR measurements were performed on an L band continuous wave (CW) EPR spectrometer (Bruker Elexsys-II E540, Germany) CW EPR spectrometer using a surface coil (Bruker, Germany). Anesthesia was induced with 3% isoflurane (Aerrane, Baxter Polska Sp. z o. o., Poland) and then maintained at 1.5 – 2.0% isoflurane in air, administered at 1.2 l/min through a nose mask. The breathing rate and rectal temperature of a subject mouse were monitored.

In vivo 2D + Spectral EPR imaging was carried out with the following parameters: microwave power = 10.75 mW; center field = 387.95 G; modulation frequency = 100 kHz; modulation amplitude = 0.7 G; maximum magnetic field gradient = 3 G/cm; number of projections = 434 (31 spatial and 14 spectral). The pO_2 images have a spatial resolution of 0.75 mm; however, signal post-processing, such as filtering and interpolation, improves image presentation, and the final pixel size is approximately 0.08 mm [25]. Acquiring one image took approximately 30 min. CP (3-Carboxy-2,2,5,5-tetramethyl-1-pyrrolidinyloxy, Sigma Aldrich, 200 μl of 50 mM solution, intraperitoneal bolus injection) was used as an oxygen-sensitive spin probe. Animals whose tumors reached an average diameter of 6 mm were qualified for the following experimental groups: OMB IV + US (tumor subjected to ultrasound impulse after intravenous administration of 100 μl of oxygen microbubbles), OMB IT + US (tumor subjected to ultrasound impulse after intratumoral administration of 20 μl of oxygen microbubbles), OMB IV (animals were administered intravenous injection of 100 μl of oxygen microbubbles, without ultrasound impulse), OMB IT (animals were administered intratumoral injection of 20 μl of oxygen microbubbles, without ultrasound impulse) and NMB IV + US (tumor subjected to ultrasound impulse after intravenous administration of nitrogen microbubbles). The application of the ultrasound (US) pulse was conducted immediately after injection of oxygen microbubbles. Recently, we have shown by means of spectroscopic EPR measurements that in the group treated by intratumoral injection of NMBs there was no significant increase in tumor pO_2 [24]. Therefore, this group was not selected for imaging and radiotherapy experiments.

The analysis of the obtained spectra was carried out using a script written in Matlab environment [26]. A Shepp-Logan filter with a cutoff frequency of 0.5, threshold 0.55 and 4-fold interpolation was used. On the data prepared in this way, a two-stage reconstruction of the two-dimensional spectroscopic image was performed. The obtained spectral widths were converted into the values of the partial oxygen pressure by using the calibration curve.

2.4. In vivo photoacoustic imaging

A high resolution photoacoustic imaging system, designed for the examination of small animals (VEVO 2100 LAZR, VisualSonics, Canada) with MS250S and LZ400 transducers was used for the study. During the imaging process, the body temperature was controlled by a heating pad and kept at 37 °C. Anesthesia was induced by 3% isoflurane (Aerrane, Baxter Polska Sp. z o. o., Poland) and then maintained at 1.5 – 2.0% isoflurane in the air, administered at 1.2 l/min using a nose mask.

First, control three-dimensional measurements were performed in the B mode (tumor morphology, transducer frequency - 40 MHz, gate - 22 dB), Power Doppler mode (tumor vasculature, transducer frequency - 32 MHz, Doppler gate - 35 dB, sensitivity - 5) and after changing the transducer to the LZ550 Oxy-Hemo photoacoustic mode. Subsequently, depending on the experimental group (OMB IV + US, OMB IT + US, OMB IV, OMB IT, NMB IV + US), the microbubble solution and ultrasound pulse were administered and a series of six three-dimensional photoacoustic measurements were made using hemoglobin as endogenous contrast agent. Each measurement took about 5 min, so the measurements were taken one after the other for 30 min. Measurements were performed in the Oxy-Hemo mode at two wavelengths of 750 and 850 nm, creating images of hemoglobin bound and unbound with oxygen. Total hemoglobin and its oxygen saturation were quantified with HemoMeaZure™ and OxyZated™ tools (VisualSonics, Canada), respectively. Tumor outline was defined in PA images by an experienced researcher manually, based on the B-mode tumor image and visible vascular structure. Oxygen saturation (sO_2%) was calculated in the tumor area as the percentage of oxygen-bound hemoglobin in total hemoglobin.

2.5. Radiotherapy

Irradiation was performed under general anesthesia. Anesthesia was induced with 3% isoflurane and then maintained at 1.5 – 2.0% isoflurane in air, administered at 1.2 l/min through a nose mask. The tumor was mechanically retracted away from the peritoneal cavity and secured with tape. The rest of the body of the mouse was covered with lead shielding. Radiotherapy was carried out using gamma radiation produced by the THERATRON 780E (MDS Canada Inc. DBA MDS Nordion, Canada) cobalt apparatus containing the cobalt isotope ^{60}Co. A total dose of 12 Gy was deposited 5 min after the injection of microbubbles or their disruption with the ultrasound pulse at a rate of 1 Gy/min. The control group without microbubble injection was also irradiated.

After the radiotherapy animals were monitored every two days. Tumors were measured with a caliper. The animals were sacrificed when the tumors reached a volume of 1.5 cm^3 or signs of decreased well-being (breathing problems, weight loss greater than 20%). Dissected lungs were snap frozen in Cryomatrix (Thermo Shandon, USA), and stored at -80 °C. All samples were cut into 7-μm sections, mounted on glass slides, fixed in cold ethanol for 1 min, and stored in PBS at 4°C. Standard hematoxylin-eosin-stained sections were evaluated for metastatic lesions under a light microscope at a magnification of 200 × .

2.6. Expression of aggressiveness markers

24 h after treatment, tumor tissue was harvested, and the expression of the proteins β-catenin and N-cadherin was determined by Western blot analysis to evaluate the molecular response to oxygen microbubbles. Briefly, the samples were mechanically homogenized (Omni TH homogenizer), in RIPA lysis buffer (Thermo Scientific, USA) and centrifuged at 16000 g at 4 °C for 25 min. The supernatant was collected, and the protein concentration of the lysate was determined by a BCA protein assay (Sigma Aldrich, USA). For Western blot analysis, equal amounts of protein were loaded for sodium dodecyl sulfate-polyacrylamide gel electrophoresis (SDS-PAGE). The protein was then transferred to a nitrocellulose membrane, blocked with PBS-T solution (PBS with 0.1% Tween-20) solution containing 5% nonfat milk, and incubated overnight at 4°C with a primary antibody against β-catenin and N-cadherin (D10A8, D4R1H, 1:1000, Cell Signaling, USA). The antibody was detected by a horseradish peroxidase conjugated secondary antibody (7074, 1:2000, Cell Signaling, USA) after an incubation of 1 h and developed with an enhanced chemiluminescence detection kit on ChemiDoc (Bio-Rad). The equal loading was confirmed by the detection of β-actin (D6A8, 1:1000, Cell Signaling, USA). An ImageJ software package was used for densitometric analysis.

2.7. Vascular morphology and perfusion assessment

The detection of vessels, pericytes and perfusion was performed using triple immunofluorescence (IF) staining. One minute before dissection, mice received an intravenous injection of Hoechst 33342 solution (15 mg/kg body weight, Sigma Aldrich, USA). 3 h after treatment, tumor tissue was harvested, snap frozen in the Cryomatrix, and stored at -80°C. All samples were cut into 7 μm sections and mounted on glass slides. The sections were air-dried for 10 min and stored at −20°C. Immunohistochemical staining was performed with rabbit anti-CD31 and rat anti-NG2 (PA5-16301, MA5-24247, 1:200, Invitrogen, USA) applied for 90 min at 37 °C. Immunodetection was performed with goat polyclonal anti-rabbit combined with Alexa Fluor 555 and chicken polyclonal anti-rat combined with Alexa Fluor 488 (A32732, A-21470, 1:200, Invitrogen, USA) for 45 min at room temperature. Photos of the slides were taken with the JuLI™ Stage camera (NanoEntek, South Korea) and dedicated software - 2400 images with a resolution of 1936 x 1456 pixels from each channel (bright field, Hoechst, Alexa Fluor 488 and Alexa Fluor 555) were automatically collected from each slide containing 9 tissue sections.

The photos were analyzed using script written in the Matlab environment. Briefly, images in three channels (red - vessels, green - pericytes, blue - Hoechst) were enhanced for contrast, binarized using the Otsu method [27] and background subtracted. Additionally, an image of dilated microvessels was prepared (using the imdilate function) and the mask of pericytes near or collocated with the vessels was calculated on its basis. On the images prepared in this way, the microvessel density (the number of vessels per tumor slice), microvessel diameter (using the regionprops function on the red channel mask), pericyte coverage (the ratio of the pericyte signal near and colocalized with microvessels to the microvessel signal), Hoechst perfused area (expressed as a percent of the whole tumor section) and Hoechst leak (Hoechst intensity normalized to vessel density).

2.8. Statistical analysis

All results were presented as mean values and standard error of the mean (SEM). Statistical analysis was performed in STATISTICA 13.1 software (Stat-Soft Inc., USA). For each parameter, the Shapiro-Wilk normality test and the Levene test were used to determine a normal distribution and equality of variances, respectively. Depending on the data, one-way or two-way analysis of variance (ANOVA) followed by Tukey's post hoc HSD test was performed. P-values smaller than 0.05 were considered statistically significant.

3. Results

3.1. Heterogeneity of oxygen delivery by OMB

The kinetics of changes in tumor oxygenation *in vivo* was investigated in six experimental groups covering both intravenous and intratumoral injection of oxygen microbubbles. Although intravenous injection is preferred in clinic, intratumoral administration has some advantages, such as increased accumulation in the tissue and the limitation of oxidative damage only to the tumor. The change in tumor oxygenation after microbubble treatment was monitored with the use of EPR and

photoacoustic imaging.

Representative tumor oxygenation maps (Fig. 1A) showed a significant increase in oxygen partial pressure in all treatment groups. Intravenous administration, whether it be microbubbles containing oxygen or nitrogen, resulted in the formation of high pO_2 regions in the vicinity of blood vessels, especially those located in the periphery of the tumor. In the case of intratumoral administration, the distribution of high partial pressure of oxygen was more homogeneous. The obtained effect is quantified in the pO_2 histograms (Fig. 1B), where a clear shift towards higher values can be observed in all treatment groups. Fig. 1C shows that the average oxygenation values of the tumors examined are significantly higher in the therapeutic groups than in the control group. Only tumors treated with nitrogen microbubbles and ultrasound impulse did not show a statistically significant response to therapy. However, the EPR imaging lasted approximately 30 min, and the values presented in the maps are averaged over this time.

Representative images of hemoglobin saturation in tumors (Fig. 2A) showed an increase in the number of areas containing fully oxygenated hemoglobin in each treatment group. The greatest effect was shown by intravenous administration of oxygen microbubbles. Similarly, like in oxygen maps, administration of bubbles itself led to a significant increase in signal at the periphery of the tumor, while treatment with ultrasound impulse also increased the signal in the inner part of the tumor. Intratumoral administration of microbubbles of oxygen resulted in only a slight increase in intratumor signal. When the tumor tissue was subjected to ultrasound pulse, an increase in hemoglobin oxygen saturation was also observed in the main supply vessels on the periphery of the tumor. The smallest effect was seen in the group treated with nitrogen microbubbles and ultrasound pulse, where the effect was only visible in the large supply vessels.

Quantitative analysis of the data obtained showed a highly heterogeneous tumor response to therapy (Fig. 2B). However, it was observed that 10 and 15 min after intravenous administration of oxygen microbubbles and the activation of the ultrasound impulse resulted in a significant increase in blood saturation. After 20 min, a significant increase in this parameter is visible in the group treated with the intratumoral injection of OMB and the ultrasound impulse. There was no significant change in the total amount of hemoglobin in the tumor in any of the experimental groups.

3.2. Vascular consequences of OMB

Due to the visible increase in oxygenation, even in the group treated with nitrogen microbubbles and ultrasound impulse without external oxygen added, the presence of additional cavitation effects was suspected in the area of the vessels. To investigate this effect, triple staining

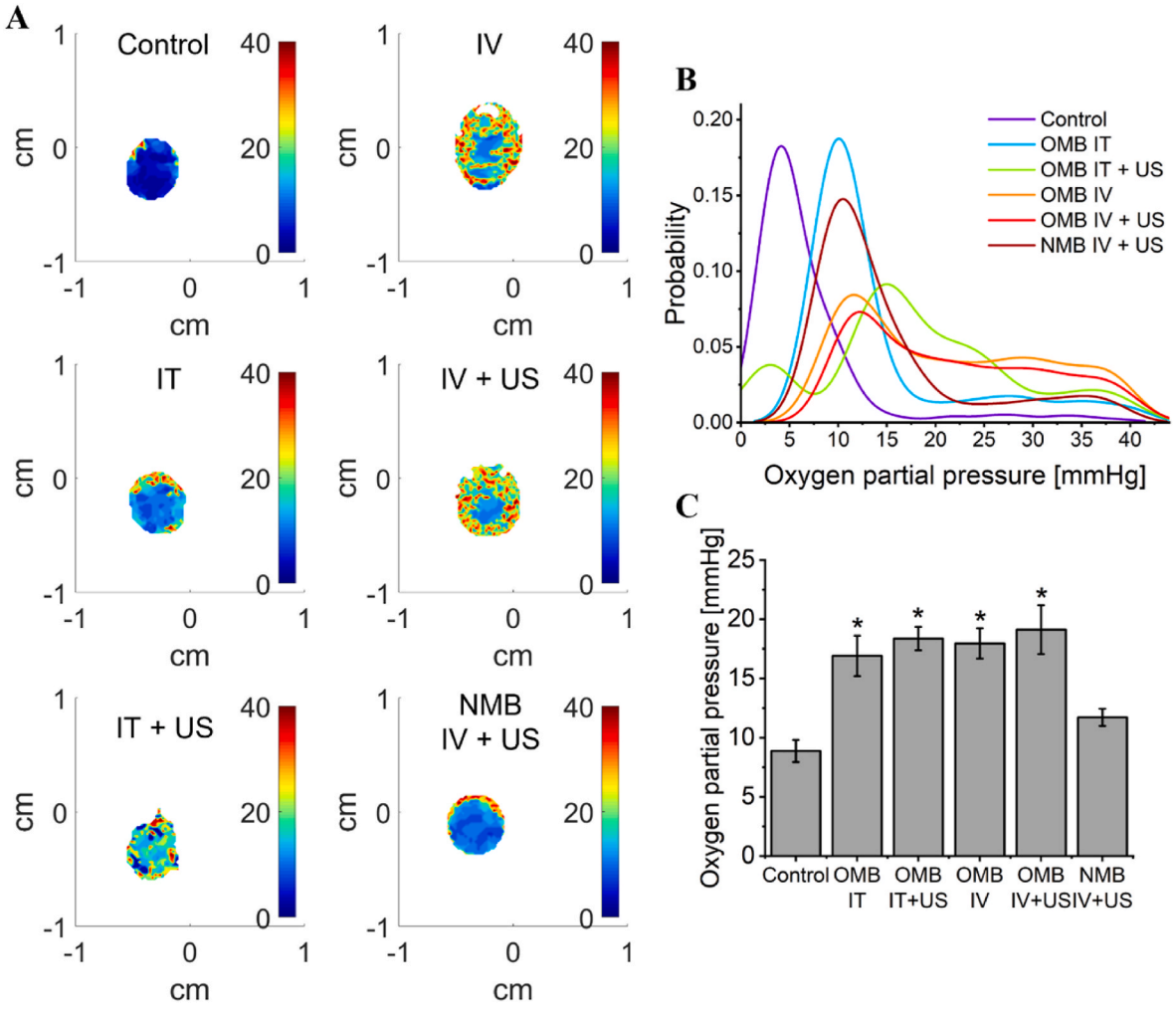

Fig. 1. In vivo EPR oxygenation imaging. A) Representative 2D tumor oxygenation maps after application of the described combinations of microbubbles (100 μl for intravenous injection and 20 μl for intratumoral injection) and ultrasound pulse (1 MHz at 2 W/cm^2 for 1 min). The color bar on the right shows pO_2 scale between 0 and 40 mm Hg. The pO_2 images have a spatial resolution of 0.75 mm; however, due to signal post-processing, the final pixel size is approximately 0.08 mm. B) Histogram of all oxygen partial pressure values in all tumors treated with oxygen/nitrogen microbubbles. C) Mean pO_2 values in the investigated experimental groups. *$p < 0.05$ relative to the control. N = 8 in each group, total N = 48. The error bars represent SEMs for the data of each group.

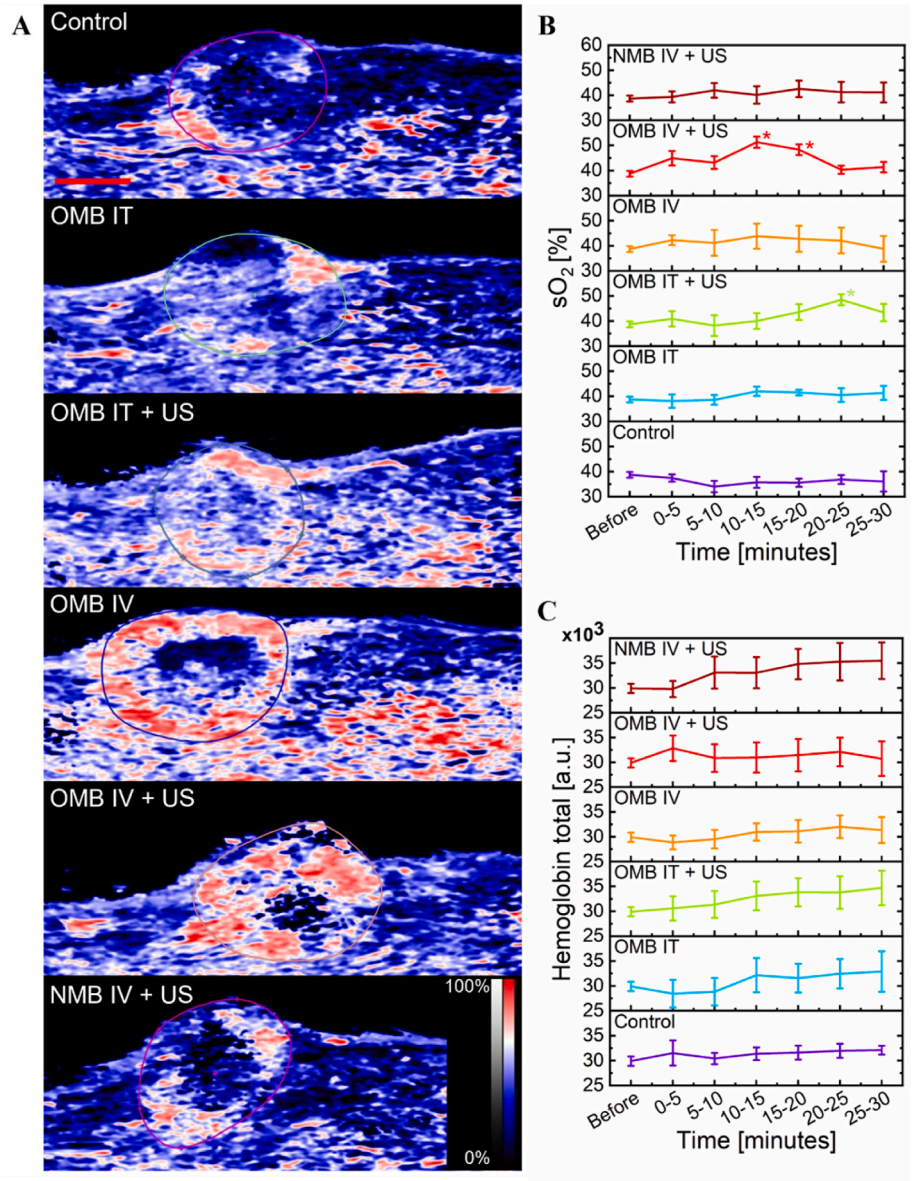

Fig. 2. Oxygenation imaging using photoacoustic imaging. A) Representative images of hemoglobin saturation in tumors from the experimental groups 10 min after treatment. The red scale bar in the first image represents 2 mm. The color scale is shown in the lower right corner and shows the percentage of hemoglobin saturation (%sO_2). B) Mean values of sO_2 oxygen saturation from the tumor area in the experimental groups. C) Mean values of total hemoglobin in the investigated experimental groups. The point before treatment represents the mean value for all groups combined. *$p < 0.05$ relative to the control. N = 8 in each group, total N = 48. The error bars represent SEMs for the data of each group. (For interpretation of the references to color in this figure legend, the reader is referred to the Web version of this article.)

for endothelial cells (localization of vessels), pericytes (well-structured mature vessels) and Hoechst dye perfusion (vessel leakage) was performed 3 h after microbubble injection/disruption in the tumor.

In Fig. 3A representative images of stained tumors from all experimental groups are presented. Hoechst dye leakage increased after microbubble therapy. Additionally, more vessels with less pericyte coverage were observed in areas of leakage. The administration of microbubbles did not affect the density or diameter of the microvessels (Fig. 3B). However, the combination of oxygen or nitrogen microbubbles with ultrasound pulse led to a significant reduction in the coverage of the vessels with pericytes. In addition, this effect is associated with a significant increase in the leakage of dye from the vessels.

The combination of oxygen and nitrogen microbubbles with the ultrasound pulse led to an increase in the permeability of the tumor vasculature. Three hours after therapy, the coverage of the vessels with pericytes decreased and dye leakage increased in the OMB IV + US and NMB IV + US groups.

3.3. Tumor radiosensitization by OMB

Oxygen is a very powerful radiosensitizer, but to see its effect, it must be present in tumor tissue at the time of radiotherapy. We tested the effectiveness of oxygen microbubbles in increasing the response of a tumor to 12 Gy gamma radiation. This dose alone cannot achieve complete tumor control, and in such applications higher doses are usually used, approximately 45–50 Gy. Furthermore, orthotopic 4T1 tumors implanted in the mammary fat pad are very close to the peritoneum and abdominal cavity, making it difficult to irradiate the tumor at high doses without significant side effects.

The kinetics of tumor growth after radiotherapy is shown in Fig. 4A. Treatment of the tumor with oxygen/nitrogen microbubbles with or without an ultrasound pulse prior to radiotherapy leads to a significant slowdown in tumor growth in all groups compared to the control treated with radiation alone. Due to premature deaths of animals as a consequence of lung metastases, the statistical significance of the plotted survival curves was not obtained (Fig. 4B). There is a significant increase in the weight of the lungs of the animals with a simultaneous decrease in the weight of the tumors (in line with the growth curve). The mean number of macroscopic lung metastases is presented in Table 1 showing an increase in the groups treated with a combination of microbubbles and ultrasound pulse. These differences were also visible in microscopic pictures of the dissected lungs, where in the groups treated with

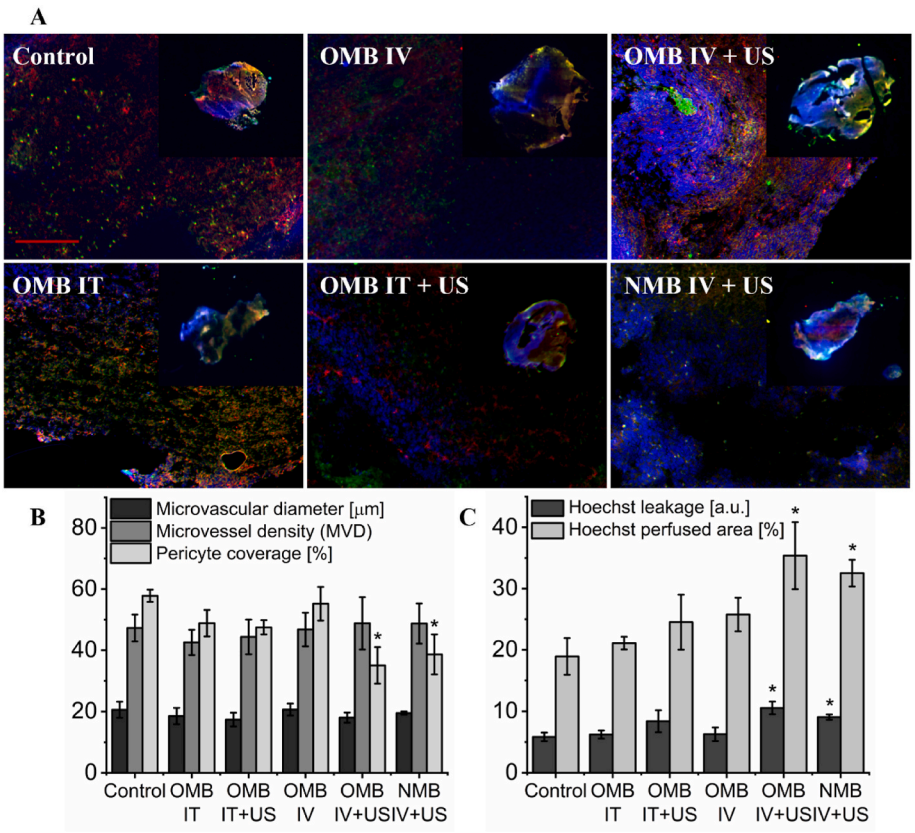

Fig. 3. Impact of microbubbles on tumor vascularization and perfusion. A) Representative fluorescent images of tumor slices from experimental groups with stained vascular endothelial cells (CD31, red), pericytes (NG2, green) and Hoechst 33342 dye perfusion (blue). The inserts in the upper right corner show the entire slice. The red scale bar in the first image represents 100 μm. Mean values of parameters determined from photos of tumor slices from the described experimental groups: B) microvessel diameter, microvessel density and vessel coverage with pericytes, C) Hoechst dye leakage and Hoechst perfused area. *$p < 0.05$ relative to the control. $N = 6$ in each group, total $N = 36$. The error bars represent SEMs for the data of each group. (For interpretation of the references to color in this figure legend, the reader is referred to the Web version of this article.)

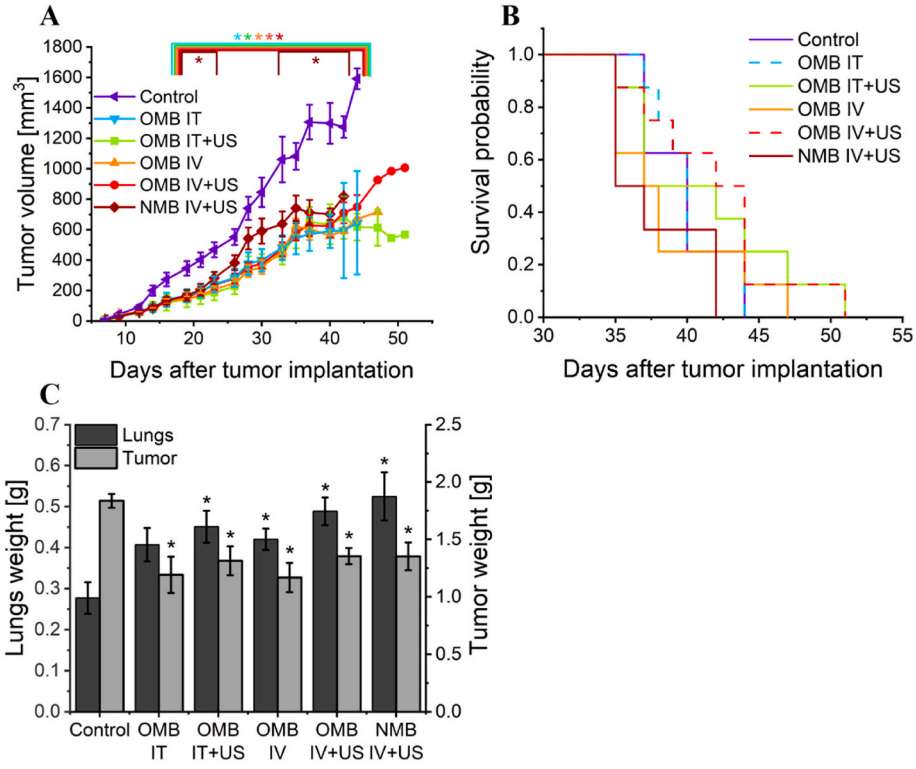

Fig. 4. Influence of microbubble therapy on the effectiveness of radiotherapy. A) Growth kinetics of 4T1 tumors treated with oxygen/nitrogen microbubbles and radiotherapy. B) Kaplan-Meier survival curves. $p = 0.11$. C) Mean weights of the lungs and tumors collected during dissection of mice from the described experimental groups. *$p < 0.05$ relative to the control. $N = 8$ in each group, total $N = 48$. The error bars represent SEMs for the data of each group.

Table 1
Mean number of macroscopic lung metastases in each experimental group with the range of days the mice were sacrificed due to tumor size or deterioration of a well-being. *p < 0.05 relative to the control.

Experimental group	Mean number of macroscopic lung metastases	Range of mice sacrifice time (days after tumor cell implantation)
Control	12 ± 2	37–44
OMB IT	15 ± 3	37–44
OMB IT + US	20 ± 4	35–51
OMB IV	18 ± 5	37–47
OMB IV + US	27 ± 8*	35–51
NMB IV + US	25 ± 4*	35–42

microbubbles and ultrasound impulse, metastatic foci were larger and more frequent (Fig. 5). Therapy with microbubbles and ultrasound pulse led to a significant increase ($p = 0.13$ and $p = 0.09$ for the OMB IV + US and NMB IV + US groups, respectively) increase in 4T1 murine breast cancer metastasis. At the time of euthanasia, the animal autopsy did not reveal other macroscopic metastatic sites other than the lung.

The effect of microbubbles on the invasiveness markers β-catenin and N-cadherin was analyzed 24 h after their injection/disruption (Fig. 6). No significant differences were detected; however, some downward trend is visible in the groups receiving microbubbles of oxygen.

4. Discussion

Microbubbles are echogenic structures consisting of a single-layer shell and a gas core. The variety of shell compositions, high surface area, loading capacity, and biocompatibility make microbubbles a promising candidate for therapeutic applications and local gas delivery [28]. Microbubbles can be used as a gas carrier alone or in combination with an ultrasound pulse to cause them to oscillate and then break down and release the gas. Moreover, the oscillations of the bubbles and their cavitation in the bloodstream or tissue lead to strong mechanical effects such as microjets and shock waves. As a result, the distribution of the drug or gas delivered by microbubbles increases significantly [29].

4.1. The spatial heterogeneity of pO_2 increase after OMB

Cancer hypoxia is a spatially and temporally heterogeneous phenomenon. This heterogeneity is the result of a combination of factors such as tumor localization, regional microvessel density, blood flow, tumor cell proliferative activity, metabolism, or disturbances in hypoxia-sensitive signaling pathways [30]. Therefore, it is necessary to visualize the spatial distribution of oxygen [31]. As in the case of our

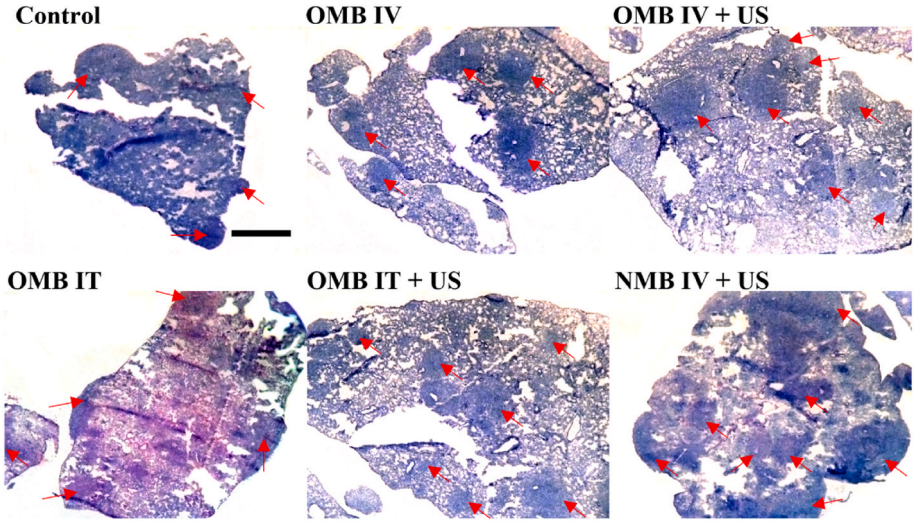

Fig. 5. Effect of microbubble therapy on 4T1 tumor metastasis. Representative photos of lung sections from the experimental groups described with distant metastases marked with red arrows. The black scale bar in the first image represents 2 mm. (For interpretation of the references to color in this figure legend, the reader is referred to the Web version of this article.)

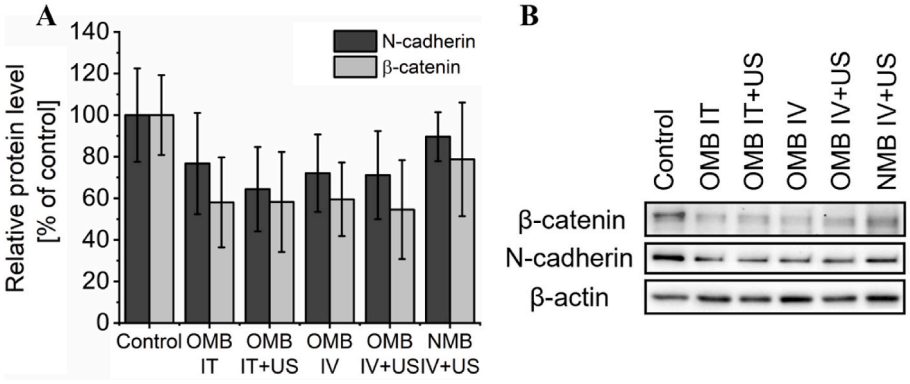

Fig. 6. Impact of oxygen microbubbles on the level of β-catenin and N-cadherin in tumor homogenates collected during dissection of mice from the experimental groups described. A) Results of the densitometric analysis normalized to β-actin. B) Representative Western Blot results for the proteins described. N = 3 in each group, total N = 18. The error bars represent SEMs for the data of each group.

previously reported spectroscopic experiments [23], intravenous and intratumoral administration of oxygen microbubbles and their combination with ultrasound pulse led to a significant increase in tumor oxygenation. Slightly higher tumor pO_2 was also observed in the group treated with nitrogen microbubbles and ultrasound, but this effect was not statistically significant. Large differences between the pO_2 values after treatment previously measured in the tumor with Oxychip (about 100 mmHg [24]) and the mean values of current oximetric imaging (about 20 mmHg) result from a longer measurement time (a few seconds for point measurement vs 30 min for imaging). Therefore, the values presented on the maps are averaged over this time. As we have previously shown, oxygen microbubbles increase tumor pO_2 for a maximum of 20 min, so the oxygen partial pressure in the image consists of both the period of pO_2 increased by the microbubbles and its decrease to the base value for 30 min. In addition, our oxygen images were acquired in two-dimensional spectral–spatial mode, representing a 2D projection of the 3D tumor volume. The resulting pO_2 values seen on the maps were averaged over tumor depth (4–6 mm). Three-dimensional imaging gives more comprehensive information about tumor microenvironment; however, in continuous wave mode and equipment that was utilized in the presented study, it requires significantly longer imaging times (approx. 1 h) which put into question physiological importance of such an approach. Despite these limitations, oximetric tumor mapping allowed the demonstration of a heterogeneous tumor response to oxygen microbubble therapy. Intravenous administration resulted in an increase in oxygen concentration, mainly in the regions of tumor vessels, while intratumoral administration resulted in more uniform growth throughout the tumor. The oxygen maps presented are the first two-dimensional pictures of the heterogeneous response to oxygen microbubbles obtained by measuring the absolute concentration of oxygen.

Photoacoustic imaging was used as a control method for the quantification of heterogeneous oxygenation of tumor tissues. In addition to invasive measurements with fiber optic probes, it is the most frequently used method in OMB research to date to assess the effectiveness of oxygen microbubbles in increasing oxygenation. However, photoacoustic measurements provide contradictory results on the action of oxygen microbubbles with a lipid shell. Some authors noted a significant increase in blood oxygen saturation that indicates the involvement of hemoglobin in oxygen transport from microbubbles [32,33], while others noted that oxygen is carried primarily through blood plasma with unchanged sO_2 [34]. The results obtained in the present study showed that compared to tissue oxygenation measurement, hemoglobin oxygen saturation did not increase to the same extent, suggesting a small contribution of hemoglobin to increasing the oxygen partial pressure. Oxygen delivery by ultrasound sensitive OMBs is largely independent of hemoglobin transport, and it results in molecular oxygen penetration of the less vascularized areas of the tumor.

4.2. Vascular disruption by microbubble cavitation

Ultrasound-mediated microbubble cavitation is widely used to increase the permeability of cells and vessels to improve the efficiency of drug and gene delivery. Microbubble cavitation not only increases intravascular shear stress leading to vasodilation, but also increases intracellular hydrogen peroxide concentration, calcium ion flux, and ATP production to regulate endothelial cell metabolism [35]. Although some authors postulate that increased drug penetration occurs for about 30 min after cavitation, reports of a longer lasting effect can also be found. Ho et al. proposed the use of oxygen microbubbles to normalize the tumor vasculature [36]. They showed that increased tumor oxygenation after treatment with oxygen microbubbles inhibited the HIF-1α/VEGF pathway, leading to an improvement in tumor vasculature morphology and function for about 2 - 8 days after single administration and destruction with 2 MPa ultrasound pulse. Pericyte coverage and Hoechst dye penetration in tumor vessels increased without changes in vessel density. Furthermore, intratumor accumulation of doxorubicin increased 3–4 times during this "normalization window". On the contrary, we observed that in the groups treated with both microbubbles and ultrasound pulse, there was a decrease in the coverage of the microvessels with pericytes and an increased penetration of Hoechst dye, indicating an increase in vascular permeability 3 h after treatment. There were no changes in the number and diameter of tumor microvessels. Although, as in the case of the authors [36], an increased leakage of the dye was observed, we postulate that OMB caused vascular disruption lasting even up to 3 h. Taking into account the results of the oximetric measurements (increase in oxygenation in the group treated with nitrogen microbubbles and ultrasound impulse) and the increased metastasis of the studied tumors after therapy, a more likely explanation for this observation is the increase in the distance between vascular endothelial cells, removal of pericytes, and probably stimulation of ceramide-dependent pathways in endothelial cells. Together, these features indicate that the increase in vessel permeability after microbubble cavitation can last for much longer than 30 min. Further research in this direction is necessary to fully describe the mechanism and relationships between these components.

4.3. Oxygen microbubbles effectively radiosensitize tumors

Oxygen microbubbles, due to the localized supply of oxygen to the tumor tissue through mechanisms that are largely independent of hemoglobin, may serve as a potential radiosensitizer. The experiments carried out showed the increased effectiveness of radiotherapy in all experimental groups. The combination of oxygen microbubbles with radiation therapy led to a significant slowdown in tumor growth compared to radiotherapy alone. There were no significant differences between the groups, which is understandable given the higher level of oxygenation (around 20 mm Hg) in the irradiated groups. This is due to the asymptotic relationship between relative radiosensitivity and oxygenation, which shows that additional oxygen delivery to tissues with pO_2 greater than 15 mmHg no longer provides a significant increase in radiation sensitivity [37].

The use of oxygen microbubbles to increase the effectiveness of radiotherapy has been shown by several research groups [32,34,38–40]. The obtained results largely agree with those demonstrated by other authors, although the range of the radiosensitization effect is quite large. This can be attributed to differences in the composition of the lipid shell of the microbubbles, the ultrasound power, and the different radiation doses and tumor models used in the research. An important contribution of our results is the action of nitrogen microbubbles, which in other studies did not show any impact on the effectiveness of radiotherapy. The observed effect, in addition to evidence from oxygen measurements, can be explained by studies analyzing the combination of perfluorocarbon microbubble cavitation with radiotherapy. The combination of microbubbles and ultrasound through cavitation effects can mechanically alter cell membranes, resulting in enhanced radiotherapy based on activation of the ceramide pathway that occurs even at low radiation doses [41]. This effect sensitizes endothelial cells to radiation through a membrane-activated cell death pathway that would otherwise be activated only at high single doses of radiation. The disruption of microbubbles by ultrasound in combination with low doses of radiation may cause acute vessel occlusion, significant cancer cell death, and reduction in tumor size. *In vivo* studies showed the effectiveness of this therapy in the treatment of breast, liver, prostate, and bladder tumors in mouse models [18]. Furthermore, these studies have led to clinical trials, in which preliminary results indicate that the combination of microbubble cavitation by ultrasound and radiotherapy is safe and causes an improved response to treatment in hepatocellular carcinoma [42].

4.4. Microbubble cavitation facilitates cancer spreading

One of the most important conclusions from experiments that

combine oxygen microbubbles and radiotherapy is the increase in metastasis of murine 4T1 breast cancer. The metastasis process of this tumor model is very well described and it is known that lung metastases begin to appear as early as 2–3 weeks after inoculation of cancer cells into the mammary fat pad and cause the death of the animals around day 35 [43]. The conducted studies showed a significant slowdown in primary tumor growth after the application of all therapeutic protocols with a simultaneous increase in the number of macroscopic pulmonary metastases. Control animals (treated only with radiotherapy) were removed from the experiment between day 38 and 44 only due to the size of the tumor (more than 1.5 cm^3) that impeded mobility. They showed no breathing problems or weight loss. On the contrary, mice in the microbubble and radiotherapy treated groups showed reduced welfare from the 35th day of the experiment, and their lungs had a higher mass and a higher number of macroscopic metastases. Of course, it should be considered that mice from these groups were sacrificed within a wide time window between 35 and 51 days of tumor growth, which, of course, may have contributed to the higher number of metastases observed simply because of the longer time available for spreading. This time window resulted from the main objective of the experiment, which was to observe inhibition of primary tumor growth. Additional experiments should be performed to understand the mechanisms associated with increased metastasis after microbubble therapy. The higher number and mass of metastases for the groups treated only with microbubbles of oxygen (without the ultrasound impulse) probably result from two times slower tumor growth and longer survival of animals, giving tumor cells more time to spread. However, all animals treated with nitrogen microbubbles and ultrasound pulse had to be removed from the experiment due to respiratory problems much earlier than control mice, and they showed about twice as many macroscopic lung metastases. This confirms that the cavitation effects are responsible for increased metastasis. Such effects of oxygen microbubbles have not been reported by other authors. So far, five publications have studied the impact of OMB on the effectiveness of radiotherapy, in which animals were monitored for a long time after administration or breakdown of the microbubbles. However, these studies used the models MDA-MB-231 (human breast cancer, nude mice, three publications) [33,34,39], CNE2 (human nasopharyngeal neoplasm, nude mice) [32] and FSA (rat fibrosarcoma) [40], which do not spontaneously metastasize.

Cancer hypoxia and activation of HIF-dependent signaling promote metastasis by regulating metabolic reprogramming, stem cell phenotype, invasion, angiogenesis, immune suppression, premetastatic niche, interaction of cancer cells with the vascular endothelium during vascular entry and exit, and resistance to apoptosis [44]. The impact of hyperoxic therapies on metastasis is still unclear. High oxygenation was shown to lead to an increase in the amount of reactive oxygen species leading to apoptosis via the MAPK pathway, a decrease in the concentration of TGF-β, or an increase in tumor infiltration with CD8 + T cells, leading to a total reduction in the number of metastases [45–47]. However, several studies focusing on hyperoxic therapies (in particular, the use of normobaric or hyperbaric carbogen or oxygen) have shown that high oxygen levels can lead to increased invasiveness of cancer cells. Crowley et al. tested the effect of a series of oxygen concentrations on breast cancer cell lines and found that a brief exposure to 60% oxygen increases their migration and promotes the secretion of several metastatic promoting factors such as VEGF, IL-8, and angiogenin [48]. Tiron et al. showed that *in vitro* exposure of breast cancer cell lines to 80% O_2 for 6 h increases ROS levels and induces the expression of VEGF-R2 and vimentin, thus promoting the epithelial-mesenchymal transition and angiogenesis [49]. *In vivo* studies in a mouse breast cancer model showed that perioperative exposure to 80% oxygen for 6 h was associated with an increased number and size of liver metastases evaluated 4 weeks after surgical resection of the tumor. The conflicting results of the presented studies can be explained by different tumor cell lines (tumor types, human and mouse tumors), oxygen concentrations, and exposure times. They also indicate that the influence of oxygen on tumor invasiveness may depend on the cellular context. In this study, a single dose of only microbubbles of oxygen led to more metastases in the lungs, while in combination with the ultrasound impulse it resulted in even greater dissemination. At the same time, 24 h after administration of oxygen microbubbles, a slight decrease in the level of markers of the invasive phenotype of cancer cells, such as β-catenin or N-cadherin, was observed. These observations indicate that the effect of increased metastasis is largely due to cavitation damage to the endothelium of tumor microvessels when ultrasound is used. By loosening the connections between endothelial cells, microbubbles made it easier for highly invasive 4T1 cells to enter the bloodstream from where they could reach the lungs. Additional studies focusing on metastasis markers are necessary to determine changes in invasiveness of cancer cells due to the investigated therapy.

Exposure of tumor cells to ultrasound-activated microbubbles can not only increase the permeability of cell membranes and endothelial layers through sonoporation, but can also destroy the tumor microenvironment directly through thermal effects and the formation of reactive oxygen species (ROS), increasing the level of oxidative stress [50]. ROS are involved in both the signaling cascade associated with HIF activation (they can induce HIF even under normoxic conditions) and the control of metastasis, but in the latter process their influence is ambiguous [51]. Although high levels of reactive oxygen species have been shown to promote tumor cell proliferation, survival, angiogenesis, and invasiveness in mouse models and human cell lines, experimental studies have shown that supplementing the diet with antioxidants leads to faster tumor growth, higher mortality, and increased metastasis. Furthermore, cellular responses to ROS depend on their type, location, and concentration [52]. The influence of microbubble cavitation or the ultrasound pulse itself on the metastasis process has not been widely studied so far. Shi et al. showed in their *in vitro* studies that microbubble destruction by an ultrasound pulse can inhibit the epithelial-mesenchymal transition of MDA-MB-231 cells by regulating the miR-200c/ZEB1 axis by microbubble-induced reactive oxygen species [53]. Zhang et al., on the other hand, did not observe an effect of commercial microbubble destruction on VX2 tumor metastasis in combination with doxorubicin chemotherapy [54]. As can be seen, the effect of microbubble cavitation on tumor invasiveness is not unequivocal and may be cell line dependent. The increase in metastasis observed in the presented study may also be associated with a higher level of oxidative stress in tumor tissue [24]. However, no oxidative damage was found in the group treated with nitrogen microbubbles and ultrasound pulse. These results indicate that reactive oxygen species alone do not contribute to increased metastasis and additional research is needed to focus on the mechanism of this process.

The disruption of the vascular endothelium by a combination of microbubbles and ultrasound pulse was shown to be predominantly caused by inertial cavitation in opposition to thermal damage. There is a strong correlation between endothelial surface damage, ultrasound pulse rarefaction pressure peak amplitudes, and inertial cavitation dose [55]. Consequently, the negative aspects of proposed oxygen microbubble therapy can be minimized by decreasing the level of inertial cavitation. Additional measurements with the use of a passive cavitation detector could help to monitor these cavitation levels and avoid inertial cavitation that leads to the spread of cancer cells.

In conclusion, our data have shown that oxygen microbubbles are an effective method of delivering oxygen to tumor tissue and lead to an increase in the effectiveness of radiotherapy. However, the cavitation effects in the area of the tumor vessels result in a greater spread of cancer cells, which hinders their clinical use. Nevertheless, several optimization steps, such as decreasing the OMB dose and ultrasound acoustic power, need to be explored in order to minimize these harmful side effects.

Declaration of competing interest

There are no conflicts of interest to declare.

Acknowledgments

We thank Prof. Agata Exner and Prof. Wojciech Froncisz for fruitful discussions and Dr Michał Gonet for providing EPR imaging reconstruction software tool. This work was supported by the grant from the National Science Centre OPUS No. 2015/17/B/NZ7/03005. The open-access publication has been supported by the Faculty of Biochemistry, Biophysics and Biotechnology under the Strategic Programme Excellence Initiative at Jagiellonian University in Krakow, Poland.

References

[1] D. Hanahan, R. a Weinberg, Hallmarks of cancer: the next generation, Cell 144 (2011) 646–674, https://doi.org/10.1016/j.cell.2011.02.013.
[2] R.H. Thomlinson, L.H. Gray, The histological structure of some human lung cancers and the possible implications for radiotherapy, Br. J. Cancer 9 (1955) 539–549, https://doi.org/10.1038/bjc.1955.55.
[3] B. Muz, P. de la Puente, F. Azab, A.K. Azab, The role of hypoxia in cancer progression, angiogenesis, metastasis, and resistance to therapy, Hypoxia (2015) 83, https://doi.org/10.2147/hp.s93413.
[4] S. Turajlic, C. Swanton, Metastasis as an evolutionary process, Science (1979) 169–175, https://doi.org/10.1126/science.aaf2784, 352 (2016.
[5] E.B. Rankin, A.J. Giaccia, Hypoxic control of metastasis, Science (1979) 175–180, https://doi.org/10.1126/science.aaf4405, 352 (2016.
[6] S.Y. Tam, V.W.C. Wu, H.K.W. Law, Hypoxia-induced epithelial-mesenchymal transition in cancers: HIF-1α and beyond, Front. Oncol. 10 (2020), https://doi.org/10.3389/fonc.2020.00486.
[7] G. Schwarz, Zur genaueren kenntnis der Radiosensibilitat, Wien Klin. Wochenschr. 11 (1910) 397–398.
[8] M.C. Joiner, A.J. van der Kogel, Basic Clinical Radiobiology, CRC Press, Fifth Edition, CRC Press/Taylor & Francis Group, Boca Raton, FL, 2018, https://doi.org/10.1201/9780429490606, 2018.
[9] P. Howard-Flanders, D. Moore, Radiation Research Society the Time Interval after Pulsed Irradiation within Which Injury to Bacteria Can Be Modified by Dissolved Oxygen: I. A Search for an Effect of Oxygen 0.02 Second after Pulsed Irradiation, 1958. http://www.jstor.orgURL. http://www.jstor.org/stable/3570768.
[10] R. Abou Khouzam, R.F. Zaarour, K. Brodaczewska, B. Azakir, G.H. Venkatesh, J. Thiery, S. Terry, S. Chouaib, The effect of hypoxia and hypoxia-associated pathways in the regulation of antitumor response: friends or foes? Front. Immunol. 13 (2022) https://doi.org/10.3389/fimmu.2022.828875.
[11] L.H. Gray, A.D. Conger, M. Ebert, R. Nat, S. Hornsey, O.C.A. Scott, B. Ch, The concentration of oxygen dissolved in tissues at the time of irradiation as a factor in radiotherapy, Br. J. Radiol. 26 (1953) 638–648.
[12] M.P. Krafft, Alleviating tumor hypoxia with perfluorocarbon-based oxygen carriers, Curr. Opin. Pharmacol. 53 (2020) 117–125, https://doi.org/10.1016/j.coph.2020.08.010.
[13] M. Xu, P. Wang, S. Sun, L. Gao, L. Sun, L. Zhang, J. Zhang, S. Wang, X. Liang, Smart strategies to overcome tumor hypoxia toward the enhancement of cancer therapy, Nanoscale 12 (2020) 21519–21533, https://doi.org/10.1039/D0NR05501H.
[14] A. sen Gupta, Hemoglobin-based oxygen carriers: current state-of-the-art and novel molecules, Shock 52 (2019) 70–83, https://doi.org/10.1097/SHK.0000000000001009.
[15] M.H. Bennett, J. Feldmeier, R. Smee, C. Milross, Hyperbaric oxygenation for tumour sensitisation to radiotherapy, Cochrane Database Syst. Rev. (2018), https://doi.org/10.1002/14651858.CD005007.pub4, 2018.
[16] I. Grgic, F. Tschanz, N. Borgeaud, A. Gupta, P.-A. Clavien, M. Guckenberger, R. Graf, M. Pruschy, Tumor oxygenation by myo-inositol trispyrophosphate enhances radiation response, Int. J. Radiat. Oncol. Biol. Phys. 110 (2021) 1222–1233, https://doi.org/10.1016/j.ijrobp.2021.02.012.
[17] J. Deprez, G. Lajoinie, Y. Engelen, S.C. de Smedt, I. Lentacker, Opening doors with ultrasound and microbubbles: beating biological barriers to promote drug delivery, Adv. Drug Deliv. Rev. 172 (2021) 9–36, https://doi.org/10.1016/J.ADDR.2021.02.015.
[18] D. Sharma, K.X. Leong, G.J. Czarnota, Application of ultrasound combined with microbubbles for cancer therapy, Int. J. Mol. Sci. 23 (2022) 4393, https://doi.org/10.3390/ijms23084393.
[19] J. Wischhusen, F. Padilla, Ultrasound molecular imaging with targeted microbubbles for cancer diagnostics: from bench to bedside, IRBM 40 (2019) 3–9, https://doi.org/10.1016/J.IRBM.2018.10.007.
[20] A. Delalande, C. Bastié, L. Pigeon, S. Manta, M. Lebertre, N. Mignet, P. Midoux, C. Pichon, Cationic gas-filled microbubbles for ultrasound-based nucleic acids delivery, Biosci. Rep. 37 (2017), 20160619, https://doi.org/10.1042/BSR20160619.
[21] J. Wu, W.L. Nyborg, Ultrasound, cavitation bubbles and their interaction with cells, Adv. Drug Deliv. Rev. 60 (2008) 1103–1116, https://doi.org/10.1016/j.addr.2008.03.009.
[22] K. Kooiman, S. Roovers, S.A.G. Langeveld, R.T. Kleven, H. Dewitte, M.A. O'Reilly, J.-M. Escoffre, A. Bouakaz, M.D. Verweij, K. Hynynen, I. Lentacker, E. Stride, C. K. Holland, Ultrasound-responsive cavitation nuclei for therapy and drug delivery, Ultrasound Med. Biol. 46 (2020) 1296–1325, https://doi.org/10.1016/j.ultrasmedbio.2020.01.002.
[23] M.S. Karthikesh, X. Yang, The effect of ultrasound cavitation on endothelial cells, Exp. Biol. Med. 246 (2021) 758–770, https://doi.org/10.1177/1535370220982301.
[24] A. Drzał, A. Delalande, G. Dziurman, M. Fournié, C. Pichon, M. Elas, Increasing oxygen tension in tumor tissue using ultrasound sensitive O2 microbubbles, Free Radic. Biol. Med. 193 (2022) 567–578, https://doi.org/10.1016/J.FREERADBIOMED.2022.11.005.
[25] S. Subramanian, N. Devasahayam, A. McMillan, S. Matsumoto, J.P. Munasinghe, K. Saito, J.B. Mitchell, G.V.R. Chandramouli, M.C. Krishna, Reporting of quantitative oxygen mapping in EPR imaging, J. Magn. Reson. 214 (2012) 244, https://doi.org/10.1016/J.JMR.2011.11.013.
[26] M. Gonet, B. Epel, M. Elas, Data processing of 3D and 4D in-vivo electron paramagnetic resonance imaging co-registered with ultrasound. 3D printing as a registration tool, Comput. Electr. Eng. 74 (2019) 130–137, https://doi.org/10.1016/j.compeleceng.2019.01.012.
[27] N. Otsu, Threshold selection method from gray-level histograms, IEEE Trans Syst Man Cybern. SMC- 9 (1979) 62–66, https://doi.org/10.1109/TSMC.1979.4310076.
[28] A. Jangjou, A.H. Meisami, K. Jamali, M.H. Niakan, M. Abbasi, M. Shafiee, M. Salehi, A. Hosseinzadeh, A.M. Amani, A. Vaez, The promising shadow of microbubble over medical sciences: from fighting wide scope of prevalence disease to cancer eradication, J. Biomed. Sci. 28 (2021) 49, https://doi.org/10.1186/s12929-021-00744-4.
[29] K. Kooiman, S. Roovers, S.A.G. Langeveld, R.T. Kleven, H. Dewitte, M.A. O'Reilly, J.-M. Escoffre, A. Bouakaz, M.D. Verweij, K. Hynynen, I. Lentacker, E. Stride, C. K. Holland, Ultrasound-responsive cavitation nuclei for therapy and drug delivery, Ultrasound Med. Biol. 46 (2020) 1296–1325, https://doi.org/10.1016/j.ultrasmedbio.2020.01.002.
[30] P. Vaupel, A. Mayer, Tumor hypoxia: causative mechanisms, microregional heterogeneities, and the role of tissue-based hypoxia markers, in: Q. Luo, L.Z. Li, D. K. Harrison, H. Shi, D.F. Bruley (Eds.), Oxygen Transport to Tissue XXXVIII, Springer International Publishing, Cham, 2016, pp. 77–86, https://doi.org/10.1007/978-3-319-38810-6_11.
[31] M. Elas, M. Krzykawska-Serda, M. Gonet, A. Kozińska, P.M. Płonka, Electron paramagnetic resonance imaging-solo and orchestra, Medical Imaging Methods: Recent Trends (2019) 1–42, https://doi.org/10.1007/978-981-13-9121-7_1/FIGURES/7.
[32] S. Peng, R. Song, Q. Lin, Y. Zhang, Y. Yang, M. Luo, Z. Zhong, X. Xu, L. Lu, S. Yao, F. Zhang, A robust oxygen microbubble radiosensitizer for iodine-125 brachytherapy, Adv. Sci. 8 (2021), https://doi.org/10.1002/advs.202002567.
[33] Y. Yao, H. Xiao, L. Zhu, Y. Gao, J. Xu, Y. Tang, Q. Wang, C. Yang, Ultrasound-mediated oxygen delivery for enhanced radiotherapy with ultrasound imaging guidance, J. Biomed. Nanotechnol. 16 (2020) 1633–1643, https://doi.org/10.1166/jbn.2020.2990.
[34] J.R. Eisenbrey, R. Shraim, J. bin Liu, J. Li, M. Stanczak, B. Oeffinger, D.B. Leeper, S. W. Keith, L.J. Jablonowski, F. Forsberg, P. O'Kane, M.A. Wheatley, Sensitization of hypoxic tumors to radiation therapy using ultrasound-sensitive oxygen microbubbles, Int. J. Radiat. Oncol. Biol. Phys. 101 (2018) 88–96, https://doi.org/10.1016/j.ijrobp.2018.01.042.
[35] J.T. Belcik, B.H. Mott, A. Xie, Y. Zhao, S. Kim, N.J. Lindner, A. Ammi, J.M. Linden, J.R. Lindner, Augmentation of limb perfusion and reversal of tissue ischemia produced by ultrasound-mediated microbubble cavitation, Circ Cardiovasc Imaging 8 (2015), https://doi.org/10.1161/CIRCIMAGING.114.002979.
[36] Y.J. Ho, S.W. Chu, E.C. Liao, C.H. Fan, H.L. Chan, K.C. Wei, C.K. Yeh, Normalization of tumor vasculature by oxygen microbubbles with ultrasound, Theranostics 9 (2019) 7370–7383, https://doi.org/10.7150/thno.37750.
[37] J. Overgaard, Hypoxic radiosensitization: adored and ignored, J. Clin. Oncol. 25 (2007) 4066–4074, https://doi.org/10.1200/JCO.2007.12.7878.
[38] Y. Yao, H. Xiao, L. Zhu, Y. Gao, J. Xu, Y. Tang, Q. Wang, C. Yang, Ultrasound-mediated oxygen delivery for enhanced radiotherapy with ultrasound imaging guidance, J. Biomed. Nanotechnol. 16 (2021) 1633–1643, https://doi.org/10.1166/jbn.2020.2990.
[39] L.J. Delaney, L. Ciraku, B.E. Oeffinger, C.E. Wessner, J. Liu, J. Li, K. Nam, F. Forsberg, D.B. Leeper, P. O'Kane, M.A. Wheatley, M.J. Reginato, J.R. Eisenbrey, Breast cancer brain metastasis response to radiation after microbubble oxygen delivery in a murine model, J. Ultrasound Med. 38 (2019) 3221–3228, https://doi.org/10.1002/jum.15031.
[40] S.M. Fix, V. Papadopoulou, H. Velds, S.K. Kasoji, J.N. Rivera, M.A. Borden, S. Chang, P.A. Dayton, Oxygen microbubbles improve radiotherapy tumor control in a rat fibrosarcoma model – a preliminary study, PLoS One 13 (2018), https://doi.org/10.1371/journal.pone.0195667.
[41] A. Al-Mahrouki, A. Giles, A. Hashim, H.C. Kim, A. El-Falou, D. Rowe-Magnus, G. Farhat, G.J. Czarnota, Microbubble-based enhancement of radiation effect: role of cell membrane ceramide metabolism, PLoS One 12 (2017), e0181951, https://doi.org/10.1371/journal.pone.0181951.
[42] J.R. Eisenbrey, F. Forsberg, C.E. Wessner, L.J. Delaney, K. Bradigan, S. Gummadi, M. Tantawi, A. Lyshchik, P. O'Kane, J. bin Liu, C. Intenzo, J. Civan, W. Maley, S. W. Keith, K. Anton, A. Tan, A. Smolock, S. Shamimi-Noori, C.M. Shaw, US-triggered microbubble destruction for augmenting hepatocellular carcinoma response to transarterial radioembolization: a randomized pilot clinical trial, Radiology 298 (2021) 450–457, https://doi.org/10.1148/RADIOL.2020202321/ASSET/IMAGES/LARGE/RADIOL.2020202321.FIG5.JPEG.
[43] K. Tao, M. Fang, J. Alroy, G.G. Sahagian, Imagable 4T1 model for the study of late stage breast cancer, BMC Cancer 8 (2008) 228, https://doi.org/10.1186/1471-2407-8-228.

[44] T. Zhang, C. Suo, C. Zheng, H. Zhang, Hypoxia and metabolism in metastasis, 87–95, https://doi.org/10.1007/978-3-030-12734-3_6, 2019.
[45] X. Qian, Q. Zhang, N. Shao, Z. Shan, T. Cheang, Z. Zhang, Q. Su, S. Wang, Y. Lin, Respiratory hyperoxia reverses immunosuppression by regulating myeloid-derived suppressor cells and PD-L1 expression in a triple-negative breast cancer mouse model, Am J Cancer Res 9 (2019) 529–545.
[46] S.M. Hatfield, J. Kjaergaard, D. Lukashev, T.H. Schreiber, B. Belikoff, R. Abbott, S. Sethumadhavan, P. Philbrook, K. Ko, R. Cannici, M. Thayer, S. Rodig, J.L. Kutok, E.K. Jackson, B. Karger, E.R. Podack, A. Ohta, M.v. Sitkovsky, Immunological mechanisms of the antitumor effects of supplemental oxygenation, Sci. Transl. Med. 7 (2015), https://doi.org/10.1126/scitranslmed.aaa1260.
[47] S.W. Kim, I.K. Kim, J.H. Ha, C.D. Yeo, H.H. Kang, J.W. Kim, S.H. Lee, Normobaric hyperoxia inhibits the progression of lung cancer by inducing apoptosis, Exp. Biol. Med. 243 (2018) 739–748, https://doi.org/10.1177/1535370218774737.
[48] P. Crowley, V. Stuttgen, E. O'Carroll, S. Ash, D. Buggy, H. Gallagher, Exposure to 60% oxygen promotes migration and upregulates angiogenesis factor secretion in breast cancer cells, Med. Gas Res. 7 (2017) 226, https://doi.org/10.4103/2045-9912.222446.
[49] A. Tiron, I. Ristescu, P.A. Postu, C.E. Tiron, F. Zugun-Eloae, I. Grigoras, Long-term deleterious effects of short-term hyperoxia on cancer progression—is brain-derived neurotrophic factor an important mediator? An Experimental Study, Cancers (Basel) 12 (2020) 688, https://doi.org/10.3390/cancers12030688.
[50] C. Su, X. Ren, F. Nie, T. Li, W. Lv, H. Li, Y. Zhang, Current advances in ultrasound-combined nanobubbles for cancer-targeted therapy: a review of the current status and future perspectives, RSC Adv. 11 (2021) 12915–12928, https://doi.org/10.1039/D0RA08727K.
[51] I.I.C. Chio, D.A. Tuveson, ROS in cancer: the burning question, Trends Mol. Med. 23 (2017) 411–429, https://doi.org/10.1016/j.molmed.2017.03.004.
[52] C.R. Reczek, N.S. Chandel, The two faces of reactive oxygen species in cancer, Annu. Rev. Cell Biol. 1 (2017) 79–98, https://doi.org/10.1146/annurev-cancerbio-041916-065808.
[53] D. Shi, L. Guo, X. Sun, M. Shang, D. Meng, X. Zhou, X. Liu, Y. Zhao, J. Li, UTMD inhibit EMT of breast cancer through the ROS/miR-200c/ZEB1 axis, Sci. Rep. 10 (2020), https://doi.org/10.1038/s41598-020-63653-w.
[54] Y. Zhang, N. Tang, L. Huang, W. Qiao, Q. Zhu, Z. Liu, Effect of diagnostic ultrasound and microbubble-enhanced chemotherapy on metastasis of rabbit VX2 tumor, Med. Phys. 48 (2021) 3927–3935, https://doi.org/10.1002/mp.14867.
[55] J.H. Hwang, J. Tu, A.A. Brayman, T.J. Matula, L.A. Crum, Correlation between inertial cavitation dose and endothelial cell damage in vivo, Ultrasound Med. Biol. 32 (2006) 1611–1619, https://doi.org/10.1016/j.ultrasmedbio.2006.07.016.